Unconventional magnetic states and defects

Barts, Evgenii

DOI:
10.33612/diss.784926551

Chapter 5

Magnetically-induced electric polarization peaks in ferrimagnetic multiferroic $Fe_{2-x}Zn_xMo_3O_8$

Abstract

A sharp increase in the electric polarization was recently observed[1] in the magnetization switching processes in the polar ferrimagnetic material, Zn-doped kamiokite, $Fe_{2-x}Zn_xMo_3O_8$. Our numerical simulations show that the magnetization reversal involves a competing antiferromagnetic phase with a higher electric polarization that intervenes between the ferrimagnetic up- and down-states. Specifically designed switching protocols may open a route to electric control of magnetization in kamiokite and related materials.

5.1 Introduction

The coupling between the ferromagnetic and ferroelectric orders in multiferroic materials can significantly reduce the energy cost of writing information in magnetic memory devices [190, 191], which prompted a quest for materials with strong magnetoelectric coupling. Electrical control of magnetic order is essential for advances in antiferromagnetic [6] and ferrimagnetic [7] spintronics.

$Fe_2Mo_3O_8$ is a mineral called kamiokite. It is a polar antiferromagnet showing a very large thermal Hall effect [157, 192, 193] and an optical diode effect [194]. Each *ab* layer of this hexagonal material has a net ferrimagnetic moment as the honeycomb spin lattice in each layer is formed by an equal number of octahedrally and tetrahedrally oxygen-coordinated Fe^{2+} ions with unequal magnetic moments and opposite orientations. The difference in magnetic moments results from an unquenched orbital contribution to the magnetic moment for the octahedral coordination, which is much larger than that on tetrahedral sites. However, the total magnetization is zero

[1] S. Ghara, E. Barts, K. Vasin, D. Kamenskyi, L. Prodan, V. Tsurkan, I. Kézsmárki, M. Mostovoy, J. Deisenhofer, Magnetization reversal through an antiferromagnetic state. *Nat. Commun.* **14**, 5174 (2023)

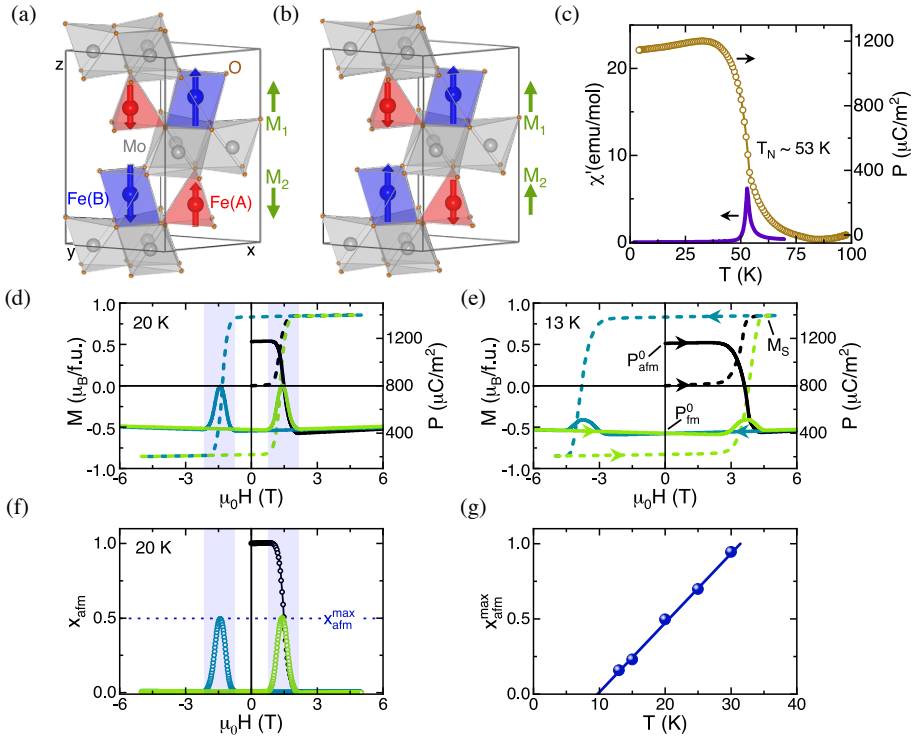

Figure 5.1: ***Summary of experimental results*** *for doped kamiokite* $Fe_{1.86}Zn_{0.14}Mo_3O_8$ *. The crystallographic unit cell contains four magnetic Fe ions with tetrahedral (red) and octahedral (blue) oxygen coordinations in the (a) antiferromagnetic and (b) ferromagnetic states. The green arrows show the net layer magnetization. (c) Temperature dependence of the magnetic susceptibility (purple) and polarization (yellow). Magnetization (dashed lines) and polarization (solid lines) under magnetic field switching are shown for (d)* $T = 20$ *K and (e)* $T = 13$ *K. (f) Field and (g) temperature dependence of the extracted volume fraction of the antiferromagnetic order. The figures are adapted from Ref. [197].*

due to the antiparallel alignment of the magnetic moments of neighboring layers in the antiferromagnetic (AFM) state. An applied magnetic field causes the transition into the ferrimagnetic (FiM) state with the co-aligned magnetic moments of neighboring layers [195, 196]. These two phases have different ferroelectric and magnetoelectric properties. The FiM phase shows a giant linear magnetoelectric effect, which is not observed in the AFM phase [195]. The electric polarization increase in the AFM state, counted from the polarization in the high-temperature paramagnetic phase, is a few times larger than that in the FiM state [195, 196].

Zn doping strongly affects the competition between parallel and antiparallel ordering

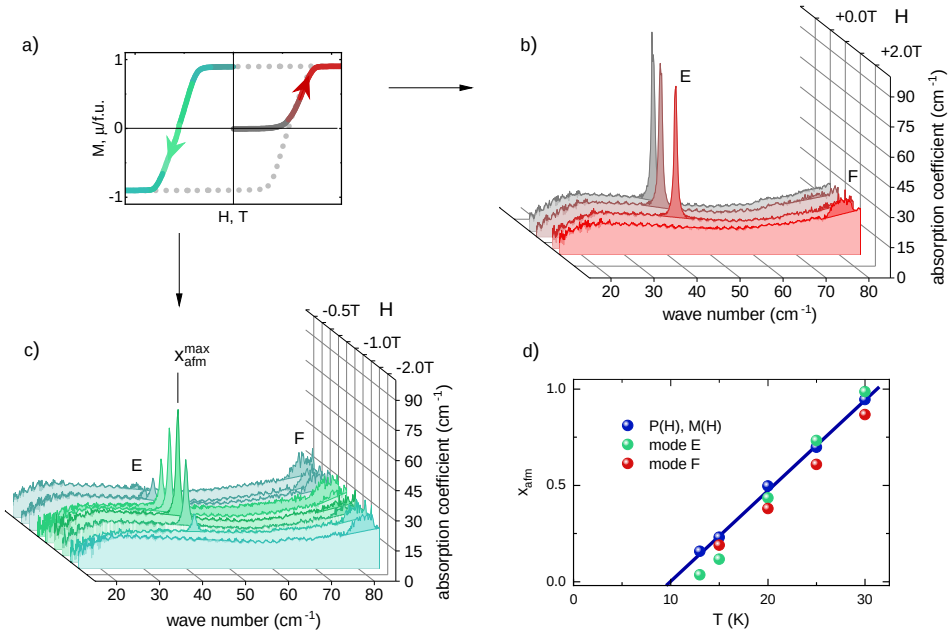

Figure 5.2: ***Summary of experimental results: THz spectroscopy***. *(a) a schematic field sweep shows the magnetic states at which THz spectra were measured. (b) The red-colored spectra indicate the fingerprints of the pristine antiferromagnetic and ferrimagnetic states named E- and F-modes, respectively. (c) The green spectra show the reappearance of these modes at the magnetization reversal. (d) The extracted maximal fraction of AFM order compared with M (H) and P (H) data in Fig. 5.1. The figure is adapted from Ref. [197].*

of the magnetic moments of neighboring layers [196]. In the lightly doped kamiokite, a sharp peak in the polarization along the crystallographic c axis was observed in the magnetization reversal processes under magnetic field sweeps [197]. Figure 5.1 summarizes the results of the recent magnetization and polarization measurements performed at the University of Augsburg. A magnon mode characteristic of the antiferromagnetic state [198] observed by THz spectroscopy is shown in Fig. 5.2.

In this chapter, we discuss the magnetic field dependence of the electric polarization of the Zn-diluted multiferroic $Fe_2Mo_3O_8$. The experimentally observed sharp peak in the polarization can be attributed to the AFM phase intervening between the FiM up and down states. The electric polarization of the AFM state is higher than that of the FiM state, which gives rise to the polarization peak. However, the magnetization changes sign at fields of the order of a few Tesla, when the AFM state is at best metastable. We perform numerical simulations of hysteresis curves to check that the

path between the down and up FiM states goes via the AFM state at a nonzero field.

The rest of the chapter is organized as follows. In Sec. 5.2, we introduce the model of Ising spins with an in-plane and a single out-of-plane exchange interaction. The model parameters are found by fitting the simulated temperature and field dependence of the magnetization with the experimental data. With this model, the magnetization reversal process is simulated at different temperatures. In Sec. 5.3, we repeat the simulation procedures for a more realistic model, wherein a half of Ising spins is replaced by more isotropic quantum spins allowing us to reproduce the experimentally observed temperature dependence of the magnetization and polarization. In Sec. 5.4, we discuss potential extensions of our study. Appendices contain technical details on simulation and an extended Ising model with three interplane exchange interactions.

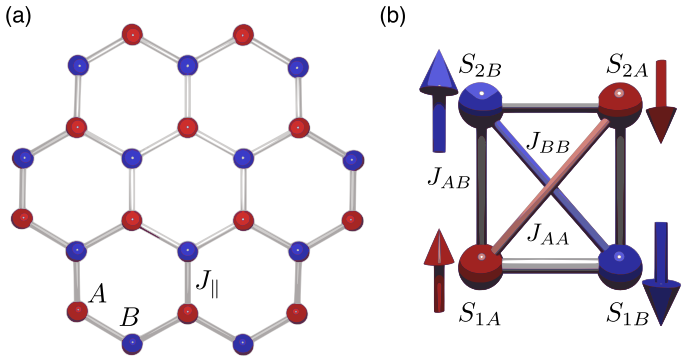

Figure 5.3: ***The kamiokite magnetic lattice structure****: (a) the honeycomb lattice of iron ions in ab layers that are stacked along the c-direction (panel b). The A (B) spin sublattice is formed by Fe ions in tetrahedral (octahedral) oxygen surrounding shown by red (blue) spheres.* $J_{\parallel}$ *(*J_{AB}, J_{AA}, J_{BB}*) are the in-plane (out-of-plane) exchange constants. The arrows show magnetic moments in the AFM state.*

5.2 Ising model

To explain the emergence of the AFM order at magnetization reversals, we consider an anisotropic Ising model of the magnetic Fe^{2+} (d^6, S=2) ions that form a honeycomb lattice in the *ab* layers. The Fe ions on A (B) sites are tetrahedrally (octahedrally) coordinated by oxygen ions, and the A and B sites alternate along the *c* direction (see

Fig. 5.3). The energy is given by

$$E = \sum_{i,j} J_{i,j}\, \boldsymbol{S}_i \cdot \boldsymbol{S}_j - H \left(M_A \sum_{i \in A} + M_B \sum_{i \in B} \right) S_i^z, \tag{5.1}$$

where the first term gives the in-plane ($J_\parallel$) and out-of-plane (J_{AB}, J_{AA}, J_{BB}) antiferromagnetic exchange interactions ($J_{i,j} > 0$), and the second term is the Zeeman energy in the magnetic field $H \| c$. The magnetic moment is $M_A = 4\mu_\mathrm{B}$, if the site belongs to sublattice A of tetrahedrally coordinated Fe ions and $M_B = 4.3\mu_\mathrm{B}$, for spins in sublattice B of octahedrally coordinated Fe ions. With these values we reproduce the experimentally observed saturation moment, $M_\mathrm{s} = 0.86\mu_\mathrm{B}$ per f.u., for $Fe_{2-x}Zn_xMo_3O_8$ with $x = 0.14$, assuming that at low temperatures, Zn substitutes Fe on tetrahedral sites [196, 199–201].

The relatively large deviation of M_B from the spin-only value $4\mu_\mathrm{B}$ results from the unquenched orbital moment of octahedrally coordinated Fe^{2+} ions, which also leads to the strong magnetic anisotropy of spins on B-sites (see Chapter 1 for details). As a result, the pure kamiokite shows a spin-flip rather than the spin-flop transition [195] in $H \| c$ expected for isotropic spins. At low temperatures, the more isotropic tetrahedral Fe spins effectively behave as Ising spins due to the strong exchange field, proportional to $J_\parallel \sim 40$ K. The exchange field is always nonzero because of the odd number of nearest-neighbor octahedral spins in the honeycomb lattice. These facts justify the use of Ising spins, $S_i^z = \sigma_i$ with $\sigma_i = \pm 1$ and $S_i^{x,y} = 0$ (the total spin $S = 2$ is absorbed in the model parameters). We also replace the interlayer couplings with a single effective ferromagnetic interaction, $J_\perp = J_{AB} - 3\frac{(J_{AA}+J_{BB})}{2} < 0$, which works well since the relatively strong nearest-neighbor AFM interactions and the large anisotropy on B-sites favor collinear spin configurations.

Figure 5.4 shows the temperature dependence of the magnetization near the Néel temperature (panel a), the AFM order parameter at the octahedral B-site sublattice $\langle L_B \rangle = \langle (S_{1B} - S_{2B})/2 \rangle$ (panel b), the specific heat, $C = \frac{\langle E^2 \rangle - \langle E \rangle^2}{k_B T^2}$ (panel c), and magnetic susceptibility, $\chi = \frac{\langle M^2 \rangle - \langle M \rangle^2}{k_B T}$ (panel d), at zero applied magnetic field and $x = 0.14$ for the minimal Ising model with the intralayer coupling $J_\parallel$ and a single interlayer coupling $J_\perp$. $J_\parallel = 40$ K was used to reproduce the observed Néel temperature, $T_N \approx 53$ K, in the doped kamiokite. The effective ferromagnetic interaction $J_\perp \ll J_\parallel$ couples A-site spins in one layer to B-site spins in a neighboring layer, which leads to an antiferromagnetic coupling between the net magnetic moments of the two layers. This weak effective coupling is a result of compensation between the three stronger antiferromagnetic interlayer interactions J_{AA}, J_{BB} and J_{AB} [202]. In undoped $Fe_2Mo_3O_8$, the coupling $J_\perp$ is related to the critical field H_cr of the spin-flip transition between the antiparallel and parallel arrangements of the magnetic moments in neighboring ab layers by $J_\perp = \frac{1}{2} H_\mathrm{cr}(M_A - M_B)$. The value $J_\perp = -0.1$ K used in

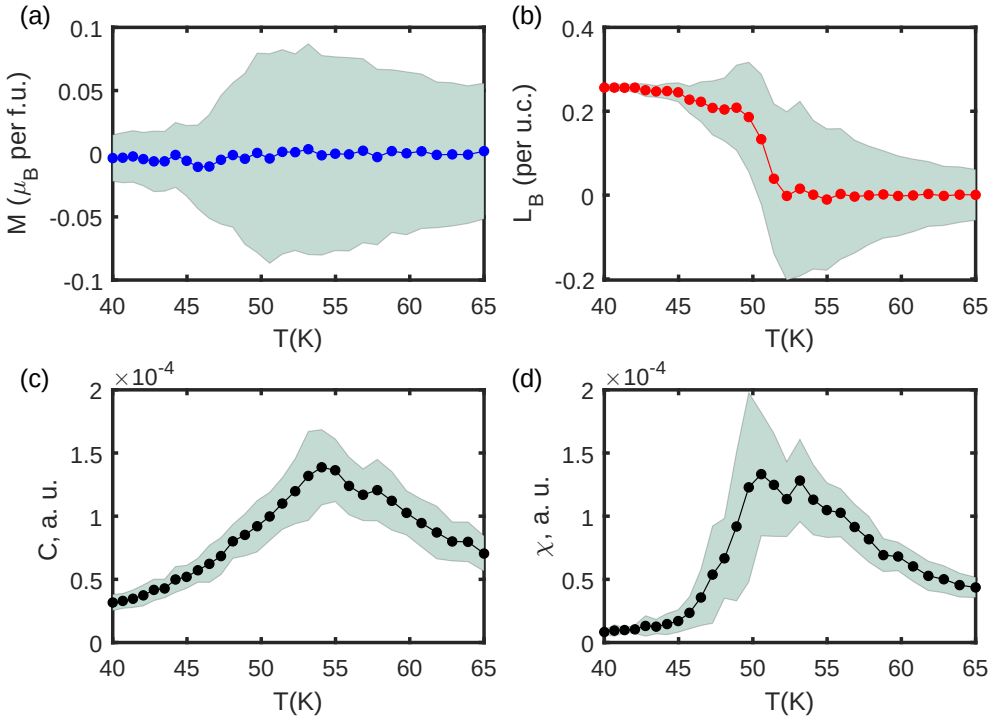

Figure 5.4: ***Critical behavior*** *of (a) the magnetization M, (b) antiferromagnetic order parameter L_B on octahedral sites, (c) specific heat C and (d) magnetic susceptibility χ, where the coloured dots are the mean values and grey shading shows the standard deviations. The model parameters are: $J_{\parallel} = 40$ K, $J_{\perp} = -0.1$ K, and $H = 0$.*

our simulations corresponds to $H_{\rm cr} = 2$ T. In reality, $H_{\rm cr}$ depends on temperature and Zn concentration [196]. This dependence can be reproduced in the model where the spins on tetrahedrally coordinated Fe ions are described as quantum $S = 2$ spins (see Sec. 5.3).

Simulations are done by employing Glauber dynamics, which is a Markov chain Monte Carlo algorithm [203, 204], used to study non-equilibrium physics in models of Ising spins. At each step, a random spin is flipped, and the flip is accepted with a probability of the weighted Boltzmann exponent, $\frac{\exp(-\Delta E/T)}{1+\exp(-\Delta E/T)}$, where ΔE is the energy difference due to the spin-flip, and T is temperature.

The initial state for the hysteresis process is prepared using the simulated annealing starting from a high-temperature ($T = 90$ K) random state. The magnetic field was increased in small increments from $0 \to 6$ T (starting for the AFM state) and from $-6 \to 8$ T (magnetization reversal). At each magnetic field value, we performed 50

measurements with $6 \cdot 10^7$ Glauber steps in-between. The results were averaged over 20-30 disorder realizations. Open boundary conditions in all three directions are used to speed up the magnetization reversal and reduce simulation time. The nonmagnetic Zn impurities are simulated by $S_i = 0$ on randomly chosen A-sites. For this simulation, the chosen temperatures were $T = 25$ K and $T = 35$ K, and the lattice has 20x10x10 unit cells (20x20x20 sites). The temperature range is covered in 30 steps in studies of critical behavior (Fig. 5.4); at each step, 50 measurements are done with $2 \cdot 10^7$ Glauber steps in-between. The final results are averaged over 48 such annealing simulations starting from a random spin configuration and randomly seeded Zn sites over the B sublattice. At each field point, the weighted averaging is done using

$$\bar{x} = \frac{\sum_i \frac{x_i}{\sigma_i^2}}{\sum_i \frac{1}{\sigma_i^2}}, \tag{5.2}$$

where x_i is a thermally averaged mean value of an order parameter, and σ_i is its standard deviation. Hence, the weight of the measured x_i-set in an individual i-sweep is $\frac{1}{\sigma_i^2}$.

The numerically calculated average magnetization M and the second power of the Néel order parameter L^2 are shown in Fig. 5.5 (a) and (b) for $T = 35$ K and $T = 25$ K, respectively. The field dependence of M is in qualitative agreement with the experimental results (see Fig. 5.1), and the maxima of L^2 near the magnetization reversals explain the observed polarization anomaly in agreement with the experiment (see Chapter 1 for the discussion of the magnetically-induced electric polarization). The magnetic curves are obtained by averaging over 24 field sweeps (see Appendix 5.5.1 for the discussion on averaging procedure for the Néel order parameter and at $T = 10$ K).

Figure 5.5 (c) shows snapshots of spin configurations in the simulated magnetic reversal. Each plane corresponds to two neighboring magnetic layers of $Fe_{2-x}Zn_xMo_3O_8$, and color describes the local magnetic ordering in the B-site sublattice: $L = (S_{B1} - S_{B2})/2 = +1$, $M = (S_{B1} + S_{B2})/2 = 0$ (red), $L = -1, M = 0$ (blue), $L = 0, M = +1$ (black), and $L = 0, M = -1$ (white). The magnetic ordering of sublattice A is essentially the same, except for the dilution due to Zn doping. The nearly uniform color of each plane reflects strong spin correlations in the *ab* layers.

We note that the model with three interplane exchange constants (J_{AB}, J_{AA}, J_{BB}) gives similar critical behavior and magnetization switching process, as shown in Appendix 5.5.2. However, that model has too many unknown parameters which cannot be fitted using the existing experimental data, and the longer-range interactions slow down the simulations.

The magnetoelectric behavior of the kamiokite is phenomenologically described by the free energy contribution

$$f_{\text{me}} = -P\left(g_L L^2 + g_M M^2 + g_H MH\right) + \frac{(P - P_0)^2}{2\chi_{\text{e}}}, \tag{5.3}$$

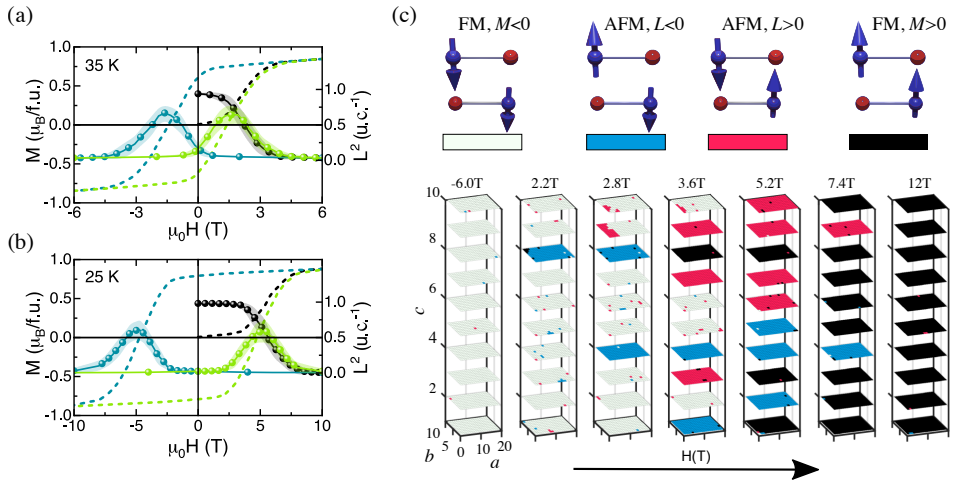

Figure 5.5: ***Simulation of magnetization reversal within the pure Ising spin model.*** *(a) Magnetic field dependence of the magnetization M (dashed lines) and the square of the AFM order parameter L^2 (solid circles) at $T = 35$ K and (b) at 25 K. (c) Snapshots of spin configurations at different magnetic fields at 25 K. Each plaquette corresponds to one unit cell of $Fe_{1.86}Zn_{0.14}Mo_3O_8$, with $M = -1, L = 0$ (white), $M = 0, L = -1$ (blue), $M = 0, L = +1$ (red) and $M = +1, L = 0$ (black), where $L = (S_1 - S_2)/2$ and $M = (S_1 + S_2)/2$, $S_{1,2}$ being B-site spins in the unit cell. These four magnetic orders are shown on top, and A-site spins are not shown for simplicity. The planes are ab layers stacked along the c axis.*

where P_0 is the electric polarization in the non-magnetic state, χ_e denotes the dielectric susceptibility, g_L and g_M describe the coupling of the electric polarization P to the AFM order parameter L and magnetization M, respectively, for spins and polarization co-aligned along the c-axis, and $g_H = \frac{\alpha}{\chi_e M_s}$ is the linear magnetoelectric coupling in the ferrimagnetic state. The minimization of f_{me} with respect to P gives

$$P = P_0 + \chi_{\mathrm{e}} \left(g_L L^2 + g_M M^2 + g_H M H \right). \tag{5.4}$$

The quadratic magnetoelectric effect $P \propto H^2$ is neglected, as it is found to be at least one order of magnitude smaller than the linear one [196].

Microscopically, the discussed magnetoelectric effect originates from exchange magnetostriction [190, 205, 206]. The induced electric polarization is due to ionic shifts giving rise to a change of valence electron wavefunction overlaps thus electron hopping integrals, $P \sim \sum_{ij} \delta J_{ij} \boldsymbol{S}_i \cdot \boldsymbol{S}_j$. Another way to induce polarization is to employ the asymmetric exchange interaction (termed inverse DMI mechanism [206]), $P \sim \sum_{ij} \delta D_{ij} \boldsymbol{S}_i \times \boldsymbol{S}_j$, provided by canted or long-range modulated spin states. However, the latter mechanism is irrelevant in the case of collinear states of strongly

anisotropic spins.

An orbital contribution to magnetization in the kamiokite manifests the ferrimagnetic order and strong magnetic anisotropy. For iron ions with octahedral oxygen coordination, the three lowest energy t_{2g} orbitals can be mapped onto the states of the fictitious orbital moment one: $(X = d_{yz}, Y = d_{zx}, Z = d_{xy})$ [52, 207],

$$\begin{aligned} &l_x X = 0, \quad l_x Y = -iZ, \quad l_x Z = iY, \\ &l_y X = iZ, \quad l_y Y = 0, \quad l_y Z = -iX, \\ &l_z X = -iY, \quad l_z Y = iX, \quad l_z Z = 0, \end{aligned} \tag{5.5}$$

which is generally expressed as $l_i = i\epsilon_{ijk} R_j \frac{\partial}{\partial R_k}$. For example, $l_x Z = -i\,(y\partial_z - z\partial_y)\,xy = izx$ and $l_z Z = -i\,(x\partial_y - y\partial_x)\,xy = -i(x^2 - y^2)$, which is zero as we projected out e_g orbitals. Importantly, the operator $(-\boldsymbol{l})$ acts on the t_{2g} triplet (X, Y, Z) in the same way as $\boldsymbol{l}$ acts on $(x, y, z) \equiv (p_x, p_y, p_z)$, since $l_i = -i\epsilon_{ijk} r_j \frac{\partial}{\partial r_k}$. This observation immediately gives the energy spectrum of the SOC Hamiltonian $H_{\mathrm{SO}} = \lambda \boldsymbol{l}\boldsymbol{s}$. In the ladder representation,

$$|\,1, \pm 1\rangle = \frac{(X \pm iY)}{\sqrt{2}}, \quad |\,1, 0\rangle = Z, \tag{5.6}$$

the lowest energy state is $|\,1, -1\rangle$ with the energy $E_{\mathrm{SO}} = -\lambda/2$. It has the largest orbital moment since $(-l_z)\,|\,1, -1\rangle = -\,|\,1, -1\rangle$. Consequently, the total magnetization of the ion acquires the orbital contribution,

$$M_z = -\mu_{\mathrm{B}}\,(L_z + 2S_z) = -5\mu_{\mathrm{B}}. \tag{5.7}$$

This equation is an incarnation of the second Hund's rule: the maximal orbital moment of electronic configuration is favored by SOC interaction. Importantly, the orbital contribution is zero for iron ions with tetrahedral ligand coordination, wherein the doublet of e_g states lie lower in energy. The orbital contribution completely quenched since l_z expectation values are always zero for the e_g doublet: $d_{3z^2-r^2} \sim |\, l_z = 0\rangle$ and $d_{x^2-y^2} \sim (|\, l_z = -2\rangle + |\, l_z = +2\rangle)$. The given above logic works for isolated ions; however, in real crystals, additional quenching appears due to interactions between ions. For the kamiokite, the orbital contribution to magnetization is only partially quenched. The large anisotropy of the first-order in SOC ($\lambda = 50$ meV for Fe ion) makes spins of Ising type. The experimentally observed giant linear magnetoelectric effect results from anisotropic corrections to g-factor.

5.3 Heisenberg-Ising model

In order to describe the temperature dependence of the spin-flip field that determines the boundary between the antiferromagnetic and ferrimagnetic states, we consider a

Heisenberg-Ising spin model:

$$E = J_{\parallel} \sum_{\langle i,j \rangle} s_i \sigma_j + J_{\perp} \sum_{i \in A} s_i \left(\sigma_{i+c/2} + \sigma_{i-c/2} \right) - H \left(\sum_{i \in A} M_A s_i + \sum_{j \in B} M_B \sigma_j \right), \tag{5.8}$$

where $s_i = S_i^z/S$ with $S_i^z = 0, \pm 1, \pm 2$, being the c-axis projection of the spin of a tetrahedrally coordinated Fe^{2+} ion ($S = 2$) in sublattice A and $\sigma_j = \pm 1$ is an Ising variable describing strongly anisotropic spins in sublattice B of octahedrally coordinated Fe ions. The first term in Eq. (5.8) is the antiferromagnetic exchange interaction ($J_{\parallel} > 0$) between neighboring spins in the ab layers forming a honeycomb lattice, the second term describes the relatively weak ferromagnetic interactions between spins in neighboring layers along the vertical AB bonds ($J_{\perp} < 0$), and the last term is the Zeeman energy for a magnetic field applied along the c axis. We use $M_B = 4.5\mu_{\rm B}$ and $M_A = 4.2\mu_{\rm B}$. With these values we reproduce the experimentally observed saturation moment, $M_{\rm s} = 0.86\mu_{\rm B}$ per f.u. assuming that Zn substitutes Fe on tetrahedral sites [196, 199–201]. We neglect the relatively weak anisotropy on A-sites.

We assume that the isotropic spins on A-sites quickly reach thermal equilibrium with the neighboring B-site spins, whereas the dynamics of the Ising spins occurs on a longer time scale and can be described by the Glauber dynamics. The sum over spin projections on tetrahedral sites, s_i, in Eq. (5.8) can be performed analytically, which leaves an effective model of Ising variables $\{\sigma_i\}$. Summing over projections of spins on A-sites, we can write the partition function of the model Eq. (5.8) in the form

$$Z = \sum_{\sigma} e^{\beta M_B H \sum_{j \in B} \sigma_j} \prod_{i \in A} z_A(h_i), \tag{5.9}$$

where $z_A(h_i) = \frac{\sinh\left(\frac{5}{4}\beta h_i\right)}{\sinh\left(\frac{1}{4}\beta h_i\right)}$ is the partition function of spin on the tetrahedral A-site i and h_i is an effective field on this site,

$$h_i = -\frac{\partial E}{\partial s_i} = -J_{\parallel} \sum_{j_{\parallel}(i)} \sigma_j + J_{\perp} \sum_{j_{\perp}(i)} \sigma_j + H M_A, \tag{5.10}$$

where $j_{\parallel}(i)$ and $j_{\perp}(i)$ labels neighboring B-sites in the same ab layer and in neighboring layers, respectively. The product $\prod_{i \in A} z_A(h_i)$ in Eq. (5.9) can be written as $e^{-\sum_{i \in A} u(h_i)}$, where $u(h_i) = -\frac{1}{\beta} \ln z_A(h_i)$ describes an induced temperature-dependent interaction between the Ising spins, as well as the interaction of the A-spin with the applied magnetic field. In particular, for $H = J_{\perp} = 0$, Eq. (5.9) becomes a partition

function of noninteracting layers of Ising spins on a triangular lattice with an effective nearest-neighbor interaction, $J_{\rm eff}(T)$:

$$e^{4\beta J_{\rm eff}(T)} = \frac{\sinh\left(\frac{15}{4}\beta h_i\right)\sinh\left(\frac{1}{4}\beta h_i\right)}{\sinh\left(\frac{5}{4}\beta h_i\right)\sinh\left(\frac{3}{4}\beta h_i\right)}. \tag{5.11}$$

The critical temperature of the two-dimensional ordering of Ising spins, T_{2D} is obtained from [208]

$$e^{\frac{4J_{\rm eff}(T_{\rm 2D})}{k_{\rm B}T_{\rm 2D}}} = 3. \tag{5.12}$$

For $T_{\rm 2D} = 60$ K (the ordering temperature of undoped kamiokite), one obtains $J_\parallel = 51.1$ K, which is used as a guess for this quasi-two-dimensional magnet. More precise values of the coupling constants $J_\parallel$ and $J_\perp$ are obtained by fitting the temperature dependence of the magnetization measured in different magnetic fields and will be discussed below (see Figs. 5.6 and 5.9).

The average magnetic moment per f.u. is given by

$$M = M_B\frac{1}{N_B}\sum_{j\in B}\sigma_j + (1-x)M_A\frac{1}{N_A}\sum_{i\in A}B_2(\beta h_i), \tag{5.13}$$

where N_A (N_B) is the number of A (B) sites, $x = 1 - \frac{N_A}{N_B}$ is the concentration of Zn dopands that substitute Fe ions on A-sites, and $B_2(x) = \frac{5}{4}\coth\frac{5x}{4} - \frac{1}{4}\coth\frac{x}{4}$ is the Brillouin function for $S = 2$. In particular, for pure kamiokite ($x = 0$)

$$M = M_B\langle\sigma\rangle + M_A\left\langle B_2(\beta h)\right\rangle. \tag{5.14}$$

At low temperatures, $\beta h \to -\infty$, independently of whether the three-dimensional ordering is ferri- or antiferro-magnetic, as the strong antiferromagnetic intralayer exchange makes A-spins antiparallel to B-spins and the applied magnetic field ($M_B > M_A$) in each *ab* layer. Therefore, the saturation magnetization of pure kamiokite (per f.u.) at low temperatures is

$$M = M_B - M_A, \tag{5.15}$$

whereas for doped kamiokite

$$M = M_B - (1-x)M_A. \tag{5.16}$$

At elevated temperatures, spins at more isotropic A-sites fluctuate more than the Ising spins on B-sites, which increases the average magnetic moment.

For hysteresis simulations, at each magnetic field value, we performed 50 measurements with 10^7 Glauber steps in-between after the waiting time of $5\cdot10^8$ steps with no measurements. The total number of field points is 32. The results were averaged over 20-30 disorder realizations. The lattice has 32x32x16 unit cells (32x32x32 Ising B-sites). All other simulation parameters are the same as in Sec. 5.2.

Our calculations show that the spin ordering in kamiokite is strongly affected by the presence of two magnetic subsystems with different magnetic moments and magnetic anisotropy. The spin-flop transition in $H\|c$ expected for isotropic spins is replaced in kamiokite by the spin-flip transition from the antiferromagnetic to ferrimagnetic phase, as discussed in Sec. 5.2. The strong AFM intralayer coupling aligns the spins of the A and B sublattices opposite to each other. However, the average magnetic moment of the *ab* layer that governs the spin-flip field depends on temperature. Since the isotropic A-site spins show stronger thermal fluctuations than the Ising spins on B-sites, the average magnetic moment decreases with increasing temperatures faster on A-sites than on B-sites. As a result, the net magnetic moment near T_N is larger than at low temperatures.

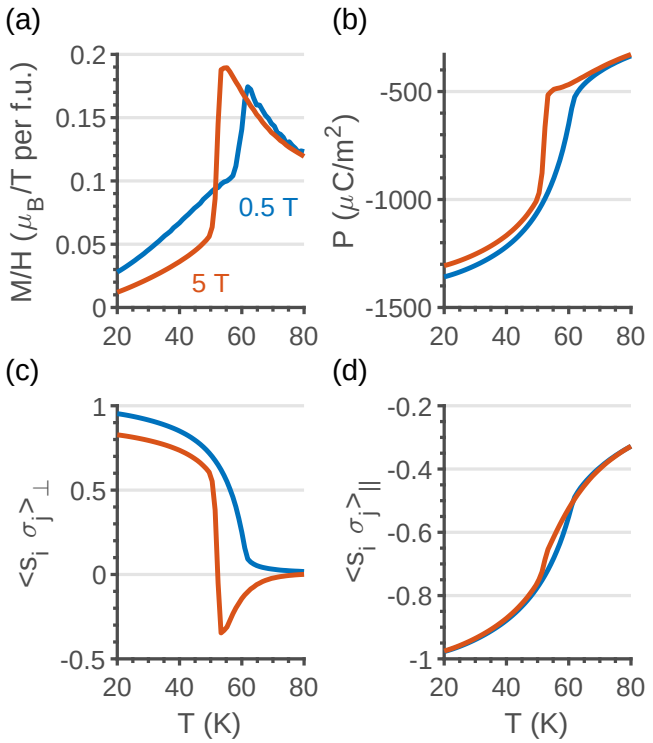

Figure 5.6: Simulated temperature dependence for undoped kamiokite: *(a) dc-susceptibility M/H, (b) polarization P and two-point spin correlators along (c) c- and (d) ab- directions for two applied fields: 5 T (red) and 0.5 T (blue). The model parameters are $J_\perp = -1.2$ K and $J_\| = 47$ K.*

The magnetoelectric behavior of $Fe_2Mo_3O_8$ is microscopically described by

$$H_{\rm me} = -g_{\parallel} P \sum_{\langle ij \rangle_{\parallel}} s_i \sigma_j - g_{\perp} P \sum_{\langle ij \rangle_{\perp}} s_i \sigma_j, \tag{5.17}$$

where $\langle ij \rangle_{\parallel}$ and $\langle ij \rangle_{\perp}$ denote nearest-neighbor pairs of spins in the same ab layer and in neighboring layers, respectively. Here, the first term describes an additional polarization induced by the intralayer ordering present in both FiM and AFM phases (and even above T_N). In contrast, the second term has different signs in the AFM and FiM states. The total polarization is

$$P = P_0 + \chi_{\rm e} \left(g_{\parallel} \sum_{\langle ij \rangle_{\parallel}} s_i \sigma_j + g_{\perp} \sum_{\langle ij \rangle_{\perp}} s_i \sigma_j \right). \tag{5.18}$$

In our simulations, the electric polarization P is counted from the polarization in the disordered high-temperature phase, hence, $P_0 = 0$. The magnetoelectric coupling constants: $\chi_{\rm e} g_{\parallel} = 1000$ μC/m^2 and $\chi_{\rm e} g_{\perp} = -400$ μC/m^2, are obtained by fitting the experimentally observed polarization temperature dependence [196].

Figure 5.6 shows the temperature dependence of the Heisenberg-Ising model for the undoped kamiokite. The field dependence of the magnetization (panel a) and electric polarization (panel b) are in good agreement with experimental data [196]. The polarization was calculated using out-of-plane $\langle s_i \sigma_j \rangle_{\perp}$ (panel c) and in-plane $\langle s_i \sigma_j \rangle_{\parallel}$ two-point spin correlation functions (panel d).

Figure 5.7 (a) shows $M(H)$ of undoped kamiokite calculated for $J_{\parallel} = 47$ K, $J_{\perp} = -1.2$ K and four different temperatures. These results are in quantitative agreement with experiment [195, 196]. The critical field necessary to flip spins just below T_N is significantly smaller than that at low temperatures, which explains the substantial increase of the spin-flip field upon decreasing temperature observed in pure kamiokite [195, 196]. The expansion of the boundary of the antiferromagnetic phase towards higher magnetic fields at low temperatures is one of the reasons for the emergence of this phase at the magnetization reversals.

The substitution of nonmagnetic Zn for Fe on tetrahedral sites increases the net magnetic moment, which further stabilizes the ferrimagnetic state reducing the critical field to zero just below T_N at $x = 0.14$. As temperature decreases, the spin-flip field increases due to the reduction of thermal fluctuations (see Fig. 5.8). In our calculations for $x = 0.14$, we used a much weaker interlayer exchange, $J_{\perp} = -0.2$ K, than for pure kamiokite to reduce the critical field value. In fact, the effective ferromagnetic coupling $J_{\perp}$ is expected to be x-dependent, as it results from the interplay between three antiferromagnetic interlayer interactions J_{AA}, J_{BB} and J_{AB} [202] depicted in Fig. 5.3. This interplay sensitively depends on the removal of magnetic ions from

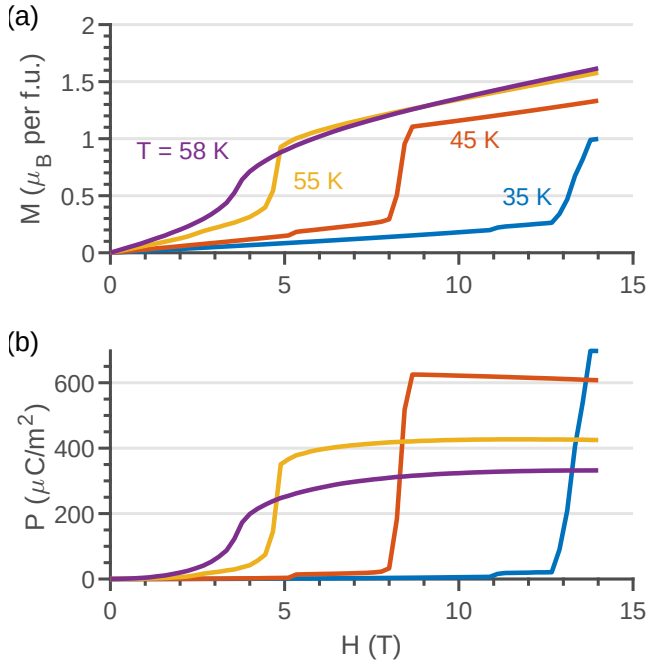

Figure 5.7: Numerically calculated $M(H)$ and $P(H)$ for pure kamiokite. *(a) field-dependence of magnetization and (b) electric polarization at $T = 58$ K (purple), 55 K (yellow), 45 K (red) and 35 K (blue). The model parameters are: $J_\perp = -1.2$ K and $J_\parallel = 47$ K.*

A-sites. The disorder averaged interplane exchange coupling is

$$J_\perp = J_{AB}(1-x) - \frac{3}{2}\left(J_{AA}(1-x)^2 + J_{BB}\right). \tag{5.19}$$

At small x, this expression correctly reproduces the decrease of the spin-flip field with doping, which is made stronger by the growth of the net magnetic moment of the ab layer upon increasing Zn concentration,

$$H_{\mathrm{SF}} = \frac{2J_\perp(x)}{\langle M_B\rangle - \langle M_A(x)\rangle}. \tag{5.20}$$

Figure 5.9 shows the temperature dependence of magnetic and ferroelectric properties of the Zn-doped kamiokite. Note that the coupling constants $g_\parallel$ and $g_\perp$ have opposite signs in our simulations. The field dependence of the electric polarization calculated for $\chi_e g_\parallel = -975$ μC/m^2 and $\chi_e g_\perp = 525$ μC/m^2 reproduces the experimentally observed polarization in the AFM and FiM states (Fig. 5.1) and its temperature dependence for $x = 0.14$ (Fig. 5.9 (b)).

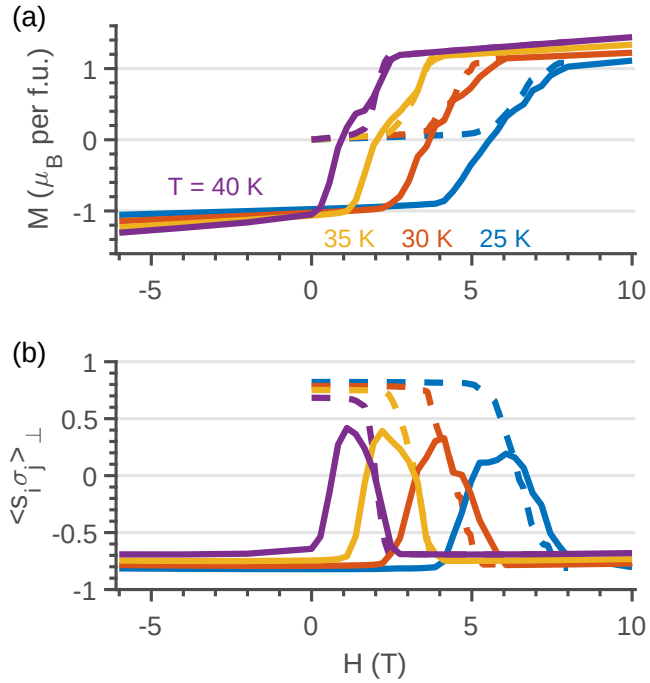

Figure 5.8: Simulated field dependence of M and P_z upon field reversal: *(a) $M(H)$ and (b) interplane correlation function $< s_i\sigma_j >_\perp$ of doped kamiokite at $x = 0.14$ (solid lines) for different temperatures: $T = 40$ K (purple), 35 K (yellow), 30 K (red) and 25 K (blue). Dashed lines show the field dependence for H varying from 0 to 14 T. The model parameters are: $J_\perp = -0.2$ K and $J_\parallel = 47$ K.*

The numerically calculated field dependence of the average magnetization M and polarization P are in qualitative agreement with the experimental results (Fig. 5.1), as shown in Fig. 5.10 (a) for $T = 25$ K and (b) for $T = 35$ K. Figure 5.10 (c) shows snapshots of spin configurations in the simulated magnetic reversal. Each plane corresponds to two neighboring magnetic layers of the kamiokite and color indicates the local magnetic ordering of the B-site sublattice: $L = (S_{B1} - S_{B2})/2 = +1$, $M = (S_{B1} + S_{B2})/2 = 0$ (red), $L = -1, M = 0$ (blue), $L = 0, M = +1$ (black), and $L = 0, M = -1$ (white). The magnetic ordering of sublattice A is essentially the same, except for the dilution due to Zn doping. The nearly uniform color of each plane reflects strong spin correlations in the *ab* layers.

The bottleneck in the magnetization reversal process is the sign change of the AFM order parameter L in an *ab* layer, which is counteracted by the strong in-plane exchange interactions. Consider a droplet of flipped spins of linear size R in a single *ab* layer.

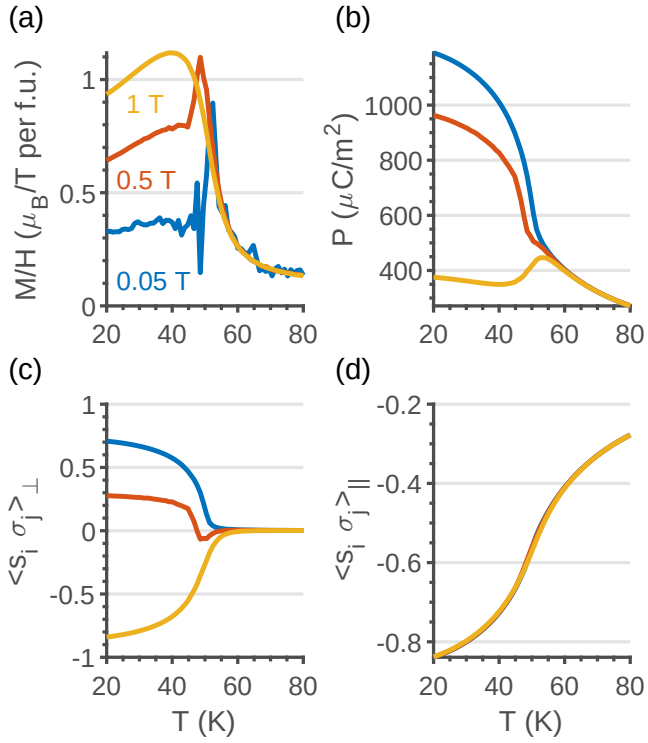

Figure 5.9: Simulated temperature dependence of magnetic and electric properties of doped kamiokite: *(a) dc-susceptibility M/H, (b) polarization P, and two-point spin correlators along (c) c- and (d) ab- directions for different applied fields: 1 T (yellow), 0.5 T (red) and 0.05 T (blue). Zn concentration is $x = 0.14$. The model parameters are $J_\perp = -0.2$ K and $J_\parallel = 47$ K.*

The free-energy of the droplet's boundary is $\sim 2J_\parallel(T)2\pi R$, where $J_\parallel(T) = J_\parallel - ck_BT$, the second term with $c \sim 1$ accounting for the boundary entropy. The corresponding energy decrease due to flipped spins is $\sim (M_A - M_B)H\pi R^2$ at low temperatures. The critical droplet size measured in lattice constants is then given by

$$R_{cr} \sim \frac{4J_\parallel(T)}{(M_B - M_A)H} = \frac{J_\parallel(T)}{|J_\perp|}\frac{H_{cr}}{H} \gg 1. \tag{5.21}$$

Droplets with $R < R_{cr}$ tend to collapse, whereas a droplet with $R > R_{cr}$ grows in size and reverses the magnetization in the entire layer. Since the formation of large droplets is improbable, the magnetization reversal occurs in steps, layer by layer, as Fig. 5.10 (c) shows.

The effect of weak interlayer interactions on the magnetization reversal is amplified

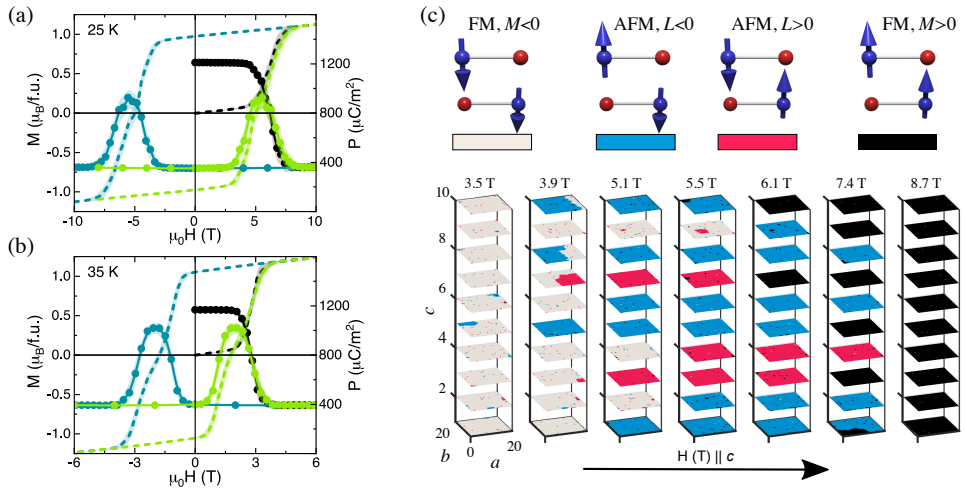

Figure 5.10: ***Simulation of spin-state evolution upon magnetization reversal for the mixed Ising-Heisenberg model.*** *(a) Magnetic field dependence of the magnetization M (dashed lines) and the polarization P at $T = 25$ K and (b) at 35 K. (c) Snapshots of spin configurations at different magnetic fields at 25 K. Each plaquette corresponds to a unit cell of $Fe_{1.86}Zn_{0.14}Mo_3O_8$, with $M = -1, L = 0$ (white), $M = 0, L = -1$ (blue), $M = 0, L = +1$ (red) and $M = +1, L = 0$ (black), where $L = (S_1 - S_2)/2$ and $M = (S_1 + S_2)/2$, $S_{1,2}$ being B-site spins in the unit cell. These four magnetic orders are shown in the top. The planes are ab layers stacked along the c axis.*

by the large critical size of the droplet. The nucleated droplet acquires additional negative energy contribution $\sim (2J_\perp)\pi R^2$, if the magnetization in two neighboring layers is not reversed. The critical size becomes

$$R_{\rm cr} \sim \frac{J_\parallel(T)}{|J_\perp|}\frac{H_{\rm cr}}{(H + H_{\rm cr})}. \tag{5.22}$$

Hence, the critical droplet is smaller and more likely to nucleate if the magnetization in the two neighboring layers is opposite to the applied field, which explains the emergence of the AFM phase at the magnetization reversals.

As temperature decreases, the magnetization reversal is delayed to high magnetic fields by the slow kinetics of Ising spins, which increases the free energy difference between the metastable AFM and the stable FiM ($M\|H$) phases. The fraction of the intervening AFM phase becomes minute, and the polarization peak decreases. This decrease is rather small in our simulations (see Fig. 5.8 (b)) since the relatively small size of the simulated lattice makes it difficult to explore AFM correlations in this quasi-two-dimensional material.

5.4 Discussion

We studied the magnetization reversal process in the antiferromagnetic kamiokite by numerically simulating Glauber dynamics of Ising spins. Our results confirm that the kamiokite's magnetization switching goes through the intermediate antiferromagnetic phase, which results in a large hump in the electric polarization. Although both the purely Ising and combined Heisenberg-Ising models explain the experimentally observed appearance of the AFM state at field reversals, the latter model gives a more accurate description of the temperature dependence of the average magnetization and electric polarization.

Our approach can be applied to other members of the kamiokite family of materials. The potential research directions are (i) effects of Fe substitutions by magnetic ions, such as Mn and Co [209–212]; (ii) heterostructures or thin-film engineering, similar to what was done for $Mn_2Mo_3O_8$ compound [213]; (iii) the use of various techniques to manipulate ferromagnetic and antiferromagnetic domains, e.g., by optical means [214, 215]. Our findings may open a route to electric control of magnetization in kamiokite and related materials.

5.5 Appendix

5.5.1 Field sweeps in the Ising model

Importantly, the straightforward averaging procedure gives zero average antiferromagnetic order parameter, $\langle L_B \rangle$, in the magnetization switching, because its sign is spontaneously chosen in each sweep. The magnitude of the AFM order parameter in most sweeps has a large peak in the interval of magnetic fields where the magnetization sign reverses (see Fig. 5.11, third column). To mitigate the spontaneous symmetry breaking effect, the AFM order parameter is multiplied by its sign at the maximal absolute value point (see Fig. 5.11, second column). Alternatively, one can introduce a small bias for the AFM order parameter. However, for the relatively small system sizes in our simulations, the required bias turns out to be comparable with the interlayer exchange interactions.

Figure 5.11 compares the magnetization reversal processes at three different temperatures: (panel a) $T = 35$ K, (panel b) $T = 25$ K and (panel c) $T = 10$ K. As discussed in the main text, the peak fraction of the AFM phase decreases with decreasing temperature, but the effect is not as prominent as in the experimental data.

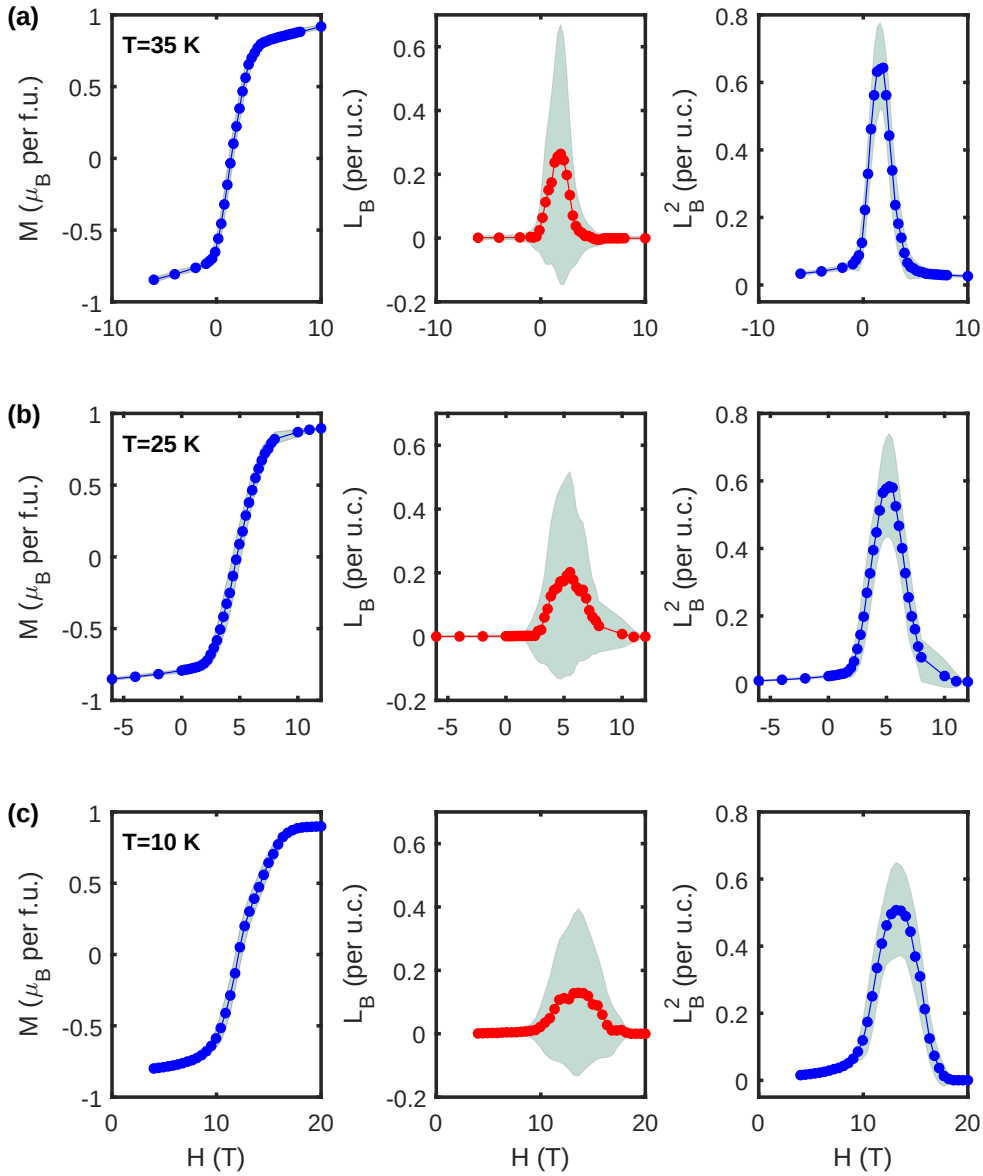

Figure 5.11: ***Field sweeps*** *of the magnetization (blue dots in the first column), sign-corrected Néel order parameter, L_B, (red dots in the second column) and the second power of the Néel order parameter L_B^2 (blue dots in third column) for (a) $T = 35$ K, (b) $T = 25$ K, (c) $T = 10$ K. Gray shading shows standard deviations.*

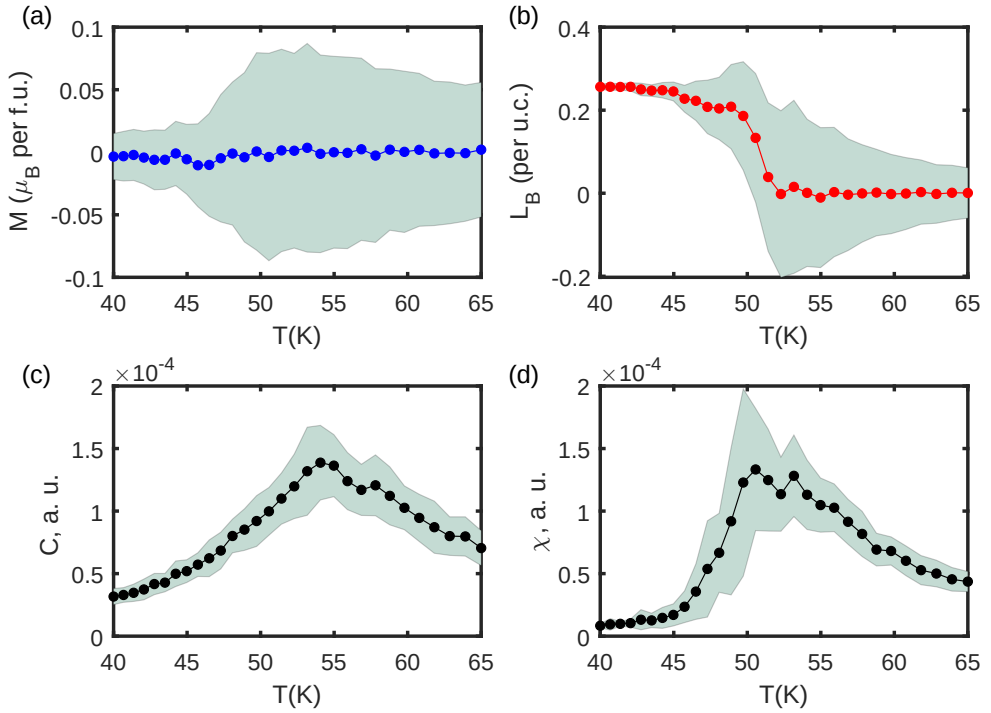

Figure 5.12: ***Critical behavior*** *of (a) the magnetization M, (b) antiferromagnetic order parameter L_B, (c) specific heat C and (d) magnetic susceptibility χ for the model with three interplane interactions. The coloured dots are the mean values and grey shading shows the standard deviations. The model parameters are: $J_{\parallel} = 40$ K, $J_{AB} = 15$ K, $J_{AA} = 5$ K, $J_{BB} = 5$ K, and $H = 0$.*

5.5.2 The Ising model with three interplane couplings

Figure 5.12 shows the critical behavior of the extended Ising model with the three interlayer exchange interactions, which agrees with the critical behavior of the single interplane exchange interaction model in Eq (5.1) (see Fig. 5.4). The model parameters are: $J_{\parallel} = 40$ K, $J_{AB} = 15$ K, $J_{AA} = 5$ K, $J_{BB} = 5$ K, which corresponds to the effective $J_{\perp} = -0.147$ K according to Eq. (5.19) in the main text. Figure 5.13 shows the field sweep for $T = 35$ K, which qualitatively agrees with Fig. 5.5 obtained within a single interplane exchange interaction.

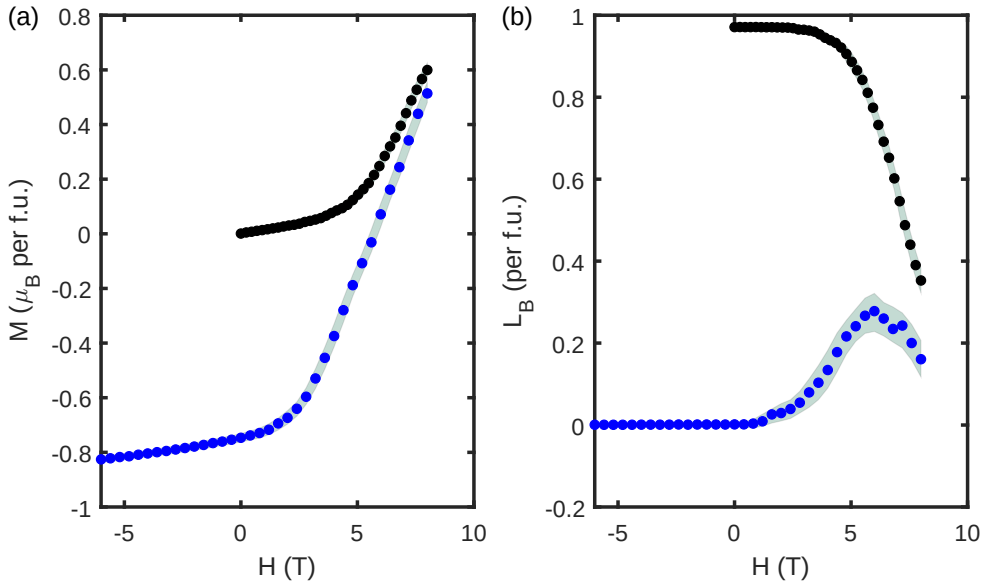

Figure 5.13: ***Field sweep curves, obtained within the model with three exchange constants*** *for the initial magnetic field $H = -6$ T (blue dots) and $H = 0$ T (black dots). Magnetic field dependence of (a) the magnetization and (b) Néel order parameter, L_B, for $T = 35$ K. Gray shading shows standard deviations. The model parameters are: $J_{\parallel} = 40$ K, $J_{AB} = 15$ K, $J_{AA} = 5$ K, and $J_{BB} = 5$ K.*